OPEN

NPG Asia Materials (2017) 9, e373; doi:10.1038/am.2017.45
www.nature.com/am

ORIGINAL ARTICLE

Single crystals of caesium formamidinium lead halide perovskites: solution growth and gamma dosimetry

Olga Nazarenko[1,2,3], Sergii Yakunin[1,2,3], Viktoriia Morad[1], Ihor Cherniukh[1] and Maksym V Kovalenko[1,2]

Formamidinium (FA)-based hybrid lead halide perovskites ($FAPbX_3$, X = I or Br/I) have recently led to significant improvements in the performance of perovskite photovoltaics. The remaining major pitfall is the instability of α-$FAPbI_3$, causing the phase transition from the desired three-dimensional cubic perovskite phase to a non-perovskite one-dimensional hexagonal lattice. In this work, we report the facile, inexpensive, solution-phase growth of cm-scale single crystals (SCs) of variable composition $Cs_xFA_{1-x}PbI_{3-y}Br_y$ ($x = 0–0.1$, $y = 0–0.6$) which exhibit improved phase stability compared to the parent α-$FAPbI_3$ compound. These SCs possess outstanding electronic quality, manifested by a high-carrier mobility–lifetime product of up to 1.2×10^{-1} $cm^2\,V^{-1}$ and a low dark carrier density that, combined with the high absorptivity of high-energy photons by Pb and I, allows the sensitive detection of gamma radiation. With stable operation up to 30 V, these novel SCs have been used in a prototype of a gamma-counting dosimeter.

NPG Asia Materials (2017) **9,** e373; doi:10.1038/am.2017.45; published online 14 April 2017

INTRODUCTION

Lead halide semiconductors with the perovskite crystal structure,[1] having the overall composition of $APbX_3$ ($A = Cs^+$, $CH_3NH_3^+$ (methylammonium or MA) or $CH(NH_2)_2^+$ (formamidinium or FA^+); $X = Cl^-$, Br^-, I^- or mixture thereof), comprise an emerging class of optoelectronic materials for applications spanning inexpensive solar cells[2–5] (with certified power conversion efficiencies exceeding 22% (http://www.nrel.gov/ncpv/images/efficiency_chart.jpg)), light-emitting diodes,[6] lasers,[7,8] broadband and narrowband photodetectors operating in the ultraviolet–visible–near infrared regions,[9,10] soft X-ray detectors[11–13] or even gamma detectors.[14,15] Such a plethora of applications is enabled, on the one hand, by the material's unique defect-tolerant photophysics,[16–19] that is, the existence of a low density of carriers (10^9–10^{11} cm^{-3}),[15,20–22] low densities of traps (10^9–10^{10} cm^{-3}),[20,23] high-carrier mobilities (25–100 $cm^2\,V^{-1}\,s^{-1}$),[15,18] and high-exciton diffusion lengths,[15,24] all despite a significant degree of structural imperfection on an atomistic scale (vacancies) and at the microscale (grain boundaries, polycrystallinity and so on). On the other hand, lead halide perovskites can also be conveniently deposited from their solutions in the form of large single crystals (SCs),[15,20,25,26] thin-films[27,28] or various nanostructured forms.[29,30] Of these forms, our focus herein is on SCs for two distinctly different reasons. First, perovskite SCs are naturally the most structurally perfect samples for fundamental studies of their intrinsic electronic and optical properties. Thus far, solution-grown SCs of $MAPbX_3$, $FAPbX_3$ and $CsPbX_3$ have been reported and their photophysical properties were characterized.[20,21,26,31–37] The second, rather practical motivation lies in the unique applicability of perovskite SCs as inexpensive, solid-state semiconductor detectors of high-energy photons (X-rays and gamma-rays).[11–15] Because most gamma radiation originates from the decay of radioactive nuclei, low-cost, sensitive and room-temperature operational radiation detectors are clearly needed for a variety of applications related to the monitoring or neutralization of major threats from the operation of nuclear reactors, terrorism or limited nuclear war, or simply for occupational safety in working with radioactive isotopes. Perovskites hold great promise as hard radiation detectors due to the compelling combination of the aforementioned electronic characteristics, the foremost of which is a high mobility–lifetime product ($\mu\tau$), and the high absorptivity of hard radiation by the high atomic number (Z) lead and iodine atoms. Such high-Z semiconductors are rarely available in single-crystalline form, explaining why CdTe and CdZnTe (CZT), grown using the complex and expensive Czochralski method, remain essentially the only materials used in commercial solid-state gamma-detectors.[38–40]

Our previous investigations of perovskite SCs for gamma photon detection focused on $MAPbI_3$, $MAPb(Br/I)_3$ and $FAPbI_3$.[14] The latter-most material, among all of those tested, was characterized by the highest $\mu\tau$ product and lowest noise level and dark current, leading to the highest gamma-counting rate. This is consistent with other reports on $FAPbI_3$ SCs, presenting a low trap density ($n_t = 1.13 \times 10^{10}$ cm^{-3}), high-carrier mobility ($\mu = 35–40$ $cm^2\,V^{-1}\,s^{-1}$),[21,35] carrier diffusion length of 6.6 μm and, importantly, low dark carrier density of 3.9×10^9 cm^{-3} (obtained by the space-charge-limited current technique).[21] $FAPbI_3$ is broadly regarded as a more chemically and thermally

[1]Department of Chemistry and Applied Biosciences, Laboratory of Inorganic Chemistry, ETH Zürich, Zürich, Switzerland and [2]Department of Advanced Materials and Surfaces, Laboratory for Thin Films and Photovoltaics, Empa—Swiss Federal Laboratories for Materials Science and Technology, Dübendorf, Switzerland
[3]These authors contributed equally to this work.
Correspondence: Professor MV Kovalenko, Department of Chemistry and Applied Biosciences, Laboratory of Inorganic Chemistry, Vladimir-Prelog-Weg 1, Zurich 8093, Switzerland.
E-mail: mvkovalenko@ethz.ch
Received 29 November 2016; revised 5 February 2017; accepted 12 February 2017

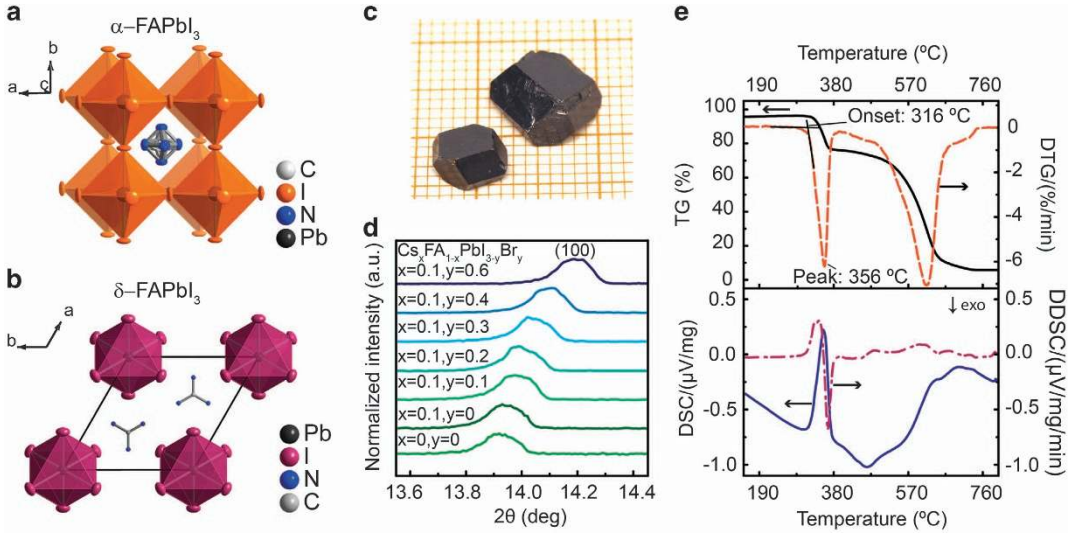

Figure 1 Growth and characterization of cesium formamidinium lead halide SCs. (**a**) Crystal structure of three-dimensional cubic α-$FAPbI_3$ (showing orientational disorder of the FA molecules).[58] (**b**) Crystal structure of one-dimensional hexagonal δ-$FAPbI_3$ (showing disorder of the nitrogen atoms down the 3-fold symmetry axis).[41] (**c**) Photographs of typical 0.5–1 cm $Cs_xFA_{1-x}PbI_{3-y}Br_y$ SCs; the smallest cell size of the paper is 1 mm × 1 mm. (**d**) X-ray powder diffraction measurements of the (100) reflection as a function of composition for $Cs_xFA_{1-x}PbI_{3-y}Br_y$ (x = 0–0.1, y = 0–0.6). (**e**) Thermal analysis of $Cs_{0.1}FA_{0.9}PbI_{2.7}Br_{0.3}$ SCs by thermogravimetry (TG, top) and differential scanning calorimetry (DSC, bottom) in flowing Ar atmosphere. The derivative of the TG and DSC curves (solid lines) are shown as dashed lines. SC, single crystal.

robust compound[34,35,41,42] than $MAPbI_3$, which decomposes to gaseous methylamine and hydrogen iodide. These beneficial attributes, along with a narrower bandgap energy, have been recognized by the photovoltaic community, leading to a gradual shift of research focus from $MAPbX_3$ thin-film absorption layers to FA-based counterparts.[42–44] However, all devices employing pure α-$FAPbI_3$ (Figure 1a) eventually suffer from its thermodynamic instability towards conversion into a wide-bandgap hexagonal (δ) phase (Figure 1b). In SCs, this cubic-to-hexagonal transformation occurs very fast, typically within 24 h after the growth of the SC.[21,33] In thin-films, this phase transformation requires from several hours to several weeks, being faster under humid atmosphere storage.[45,46] This instability has recently been fully resolved for thin-films via the formation of mixed-ionic compositions with Cs and MA, such as in $Cs_{0.17}FA_{0.83}(PbI_{1-x}Br_x)$ (x = 0–1) or $(FAPbI_3)_{1-x}(MAPbBr_3)_x$ (x = 0–0.3).[47–50] Such compositional tuning can stabilize the cubic structure via adjustment of the so-called Goldschmidt tolerance factor,[51] determined by the radii of the constituting ions, and via the entropy of mixing.[49]

In this study, we sought to obtain and characterize FA-based perovskite SCs and study their photophysical properties. Taking lessons from the photovoltaic research discussed above,[47–50] we targeted quaternary $Cs_xFA_{1-x}PbI_3$ and quinary $Cs_xFA_{1-x}PbI_{3-y}Br_y$ compositions (x = 0–0.1, y = 0–0.6). After growing cm-scale SCs (Figure 1c), and examining their structure (Figure 1d) and thermal stability (Figure 1e), we explored their gamma-counting capabilities. All of the obtained SCs were crystallized in the cubic perovskite lattice; they were found to be phase pure and possess composition-dependent bandgap energies and luminescence maxima in the range of 755–832 nm, blue-shifted compared to $FAPbI_3$ (840 nm). These compositions were also found to exhibit significantly improved phase stability, with shelf lives (the time before hexagonal phase impurities could be detected) of up to 20 days for quaternary $Cs_xFA_{1-x}PbI_3$ SCs and of >4 months for quinary $Cs_xFA_{1-x}PbI_{3-y}Br_y$ SCs. These SCs possess outstanding electronic quality, manifested by an unusually high-carrier mobility × lifetime product ($\mu\tau$) of up to 10^{-1} cm^2 V^{-1}, electronic stability under an applied bias of up to 30 V and sensitive gamma detection. Using SCs of $Cs_xFA_{1-x}PbI_{3-y}Br_y$, we also present an inexpensive prototype of a gamma-counting dosimeter.

METHODS

Chemicals and reagents

Lead (II) iodide (PbI_2, 99%), formamidine acetate (FA(OAc), 99%) and γ-butyrolactone (GBL, ⩾99%) were purchased from Sigma-Aldrich (Steinheim, Germany). Lead (II) bromide ($PbBr_2$, 98+%) was purchased from Acros (Geel, Belgium). Cesium iodide (CsI, 99.9%) and hydrogen iodide (57%, stabilized with 1.5% hypophosphorous acid) were purchased from ABCR (Karlsruhe, Germany). All chemicals were used as received without further purification.

Synthesis of formamidinium iodide (FAI)

FAI was synthesized via the reaction of FA(OAc) with an excess of hydrogen iodide (57%) upon stirring in an ice bath for 2 h. Subsequently, the solution was dried in a rotary evaporator under vacuum and mild heating (50 °C). The crude product was washed with diethyl ether and recrystallized from ethanol. After drying in a vacuum oven (overnight at 55 °C) a white powder was obtained. Single crystals of FAI, grown via the diffusion of diethyl ether into an ethanol solution of FAI, were used for structure determination (Supplementary Figure 1, for crystallography tables see Supplementary Tables 1–4). The overall purity of the obtained FAI material was confirmed by X-ray powder diffraction (Supplementary Figure 2).

Growth of perovskite SCs

$Cs_xFA_{1-x}PbI_{3-y}Br_y$ (x = 0–0.1, y = 0–0.6) were grown using the inverse temperature crystallization technique, initially reported for $FAPbI_3$ by Bakr *et al.*[33] Typically, for $Cs_xFA_{1-x}PbI_{3-y}Br_y$ (x = 0–0.1, y = 0–0.4) a 0.9 M (referring to Pb) solution of CsI/FAI/PbX_2 in GBL, prepared simply by dissolving the powders of three corresponding compounds, was used. All solutions were filtered through a 0.2 μm polytetrafluoroethylene syringe filter. To grow $Cs_{0.1}FA_{0.9}PbI_{2.4}Br_{0.6}$ SCs, the concentration was lowered to 0.8 M and solution was not filtered. Typically, 4 ml of the precursor solution were filled into a 20 ml vial with a cap and the vial was placed into a preheated (80 °C) glycerol bath. The temperature was elevated in small steps of 5 °C h^{-1} to

125–130 °C, and maintained at this point for 1 h. SCs nucleated and grew during this heating ramp. To avoid overheated areas on the bottom of the vial (to obtain fewer seeds), the vial was lifted off the bottom of the bath (fixed in a clamp) and the glycerol level was adjusted to be a few mm lower than the level of the crystallization solution. The temperature was monitored using a thermometer or thermocouple connected to the hotplate.

X-ray diffraction

Powder X-ray diffraction patterns were collected from grinded crystals in transmission geometry (Debye-Scherrer geometry) with a STADI P diffractometer (STOE & Cie GmbH, Darmstadt, Germany), equipped with a silicon strip MYTHEN 1K Detector (Fa. DECTRIS) with a curved Ge (111)-Monochromator (CuKα_1, $\lambda = 1.54056$ Å). Single-crystal X-ray diffraction measurements were conducted on Bruker Smart Platform diffractometer equipped with a Apex I CCD detector and molybdenum (MoKα, $\lambda = 0.71073$ Å) sealed tube as an X-Ray source. Crystals were tip—mounted on a micromount with paraffin oil. Data was processed and refined with APEX2 (Bruker software) and Olex2 software (Durham University).

Thermal analysis

DSC and TG analyses were performed using a Netzsch Simultaneous Thermal Analyzer (STA 449 F5 Jupiter, Selb, Germany). A powdered sample (10 mg) was placed in an alumina crucible under Ar/N_2 gas flow (50 ml min^{-1}) and heated to 850 °C (at 10 °C min^{-1}).

Optical measurements

Ultraviolet–visible absorption spectra of powdered samples held between two glass slides were collected using a Jasco V670 spectrometer equipped with an integrating sphere. Photoluminescence measurements were performed with a Fluorolog iHR 320 Horiba Jobin Yvon spectrofluorometer equipped with a Xe lamp and a photomultiplier tube.

Elemental analysis

Elemental analysis (CHN) was performed by the standard combustion method, where carbon (as CO_2) and hydrogen (as H_2O) are analysed quantitatively by infrared spectroscopy and nitrogen (N_2) is determined by a thermal conductivity detector. The halogens (Br and I) were quantified by the Schöniger method, where they are collected in an absorbing liquid medium and then analysed by titration.

Photoresponse measurement

For the evaluation of the mobility–lifetime product, $\mu\tau$, a current–voltage measurement was obtained by a Keithley 236 SMU in the dark and then under infrared light at $\lambda = 850$ nm. Being at the low-energy tail of the absorption spectrum, this wavelength corresponds to a large penetration depth of ~1 cm, similar to that of gamma photons with an energy of 300 keV.

Gamma-ray absorption measurements

The absorption of gamma radiation was measured for a set of perovskite SCs with a thickness of 0.2–15 mm. Gamma radiation from ^{241}Am and ^{137}Cs sources was collimated with a lead aperture having a diameter of 6 mm and a thickness of 5 cm. The intensity of gamma radiation transmitted through the perovskite SC was measured with a CZT detector (model B1758, eV Products, Saxonburg, PA, USA).

Gamma-detection measurements using perovskite SCs

A custom-made test fixture was used for energy-resolved measurements, connected to a A250CF CoolFET charge sensitive preamplifier (Ametek, Bedford, MA, USA), coupled with an amplifier-shaper (Model 572, EG&G Ortec, Oak Ridge, TN, USA) and a digital multichannel analyzer MCA-8000D (Ametek). The high bias voltage was applied through a Keithley 236 SMU that was also used for monitoring the current through the SC detector. ^{241}Am and ^{137}Cs gamma sources with activities of 0.4 and 2.2 MBq, respectively, were used for recording the energy spectra. For demonstration purposes, a prototype of a portable dosimeter based on a perovskite SC was connected to a preamplifier (eV Products) and a custom-made amplifier based on one stage of a LM358N chip. The gamma pulses were recorded with a digital counting board using an Arduino microprocessor set, based on an open-source project (https://sites.google.com/site/diygeigercounter/). Detector SCs were biased at 9 V by a NiMH battery.

RESULTS

Solution-growth, structure and thermal analysis of $Cs_xFA_{1-x}PbI_{3-y}Br_y$ ($x = 0$–0.1, $y = 0$–0.6)

The SCs were grown at 95–130 °C in γ-butyrolactone (GBL), using a modified inverse temperature crystallization (ITC) method (see details in the Experimental Section) (Figure 1) , similarly to the original ITC method reported for $FAPbI_3$ and $FAPbBr_3$ by Bakr *et al.*[33] In this method, the nucleation and fast growth of crystals occur upon heating, as opposed to commonly used cooling-induced supersaturation techniques. In ITC, the rare occurrence of a decrease in solubility upon heating (retrograde solubility) is exploited to induce crystallization.[52] For $FAPbI_3$ in GBL, such unusual solubility behavior was suggested to be caused by the dissociation of solvent-precursor complexes at elevated temperatures, causing oversaturation.[31,33] Recent success in thinness- and shape-controlled growth of $MAPbX_3$ SCs for inch-sized photoelecronic devices on the inch-scale speaks volumes for the versatility of an ITC method.[53,54] The modification of an ITC method, used for growth of $FAPbX_3$, implemented in this work, lies in the use of cesium iodide as the Cs-source and lead bromide as the Br-source. The overall concentration of A-type cations (FA+Cs), Pb cations and halide anions (Br+I) was maintained at 0.9, 0.9 and 2.7 M, respectively. Experimentally, a notable challenge was to prevent the formation of a yellow, non-perovskite $CsPbI_3$ phase, often occurring for $x \geqslant 0.1$. Neat GBL remained the best solvent, following trials using dimethylsulfoxide or dimethylformamide as additives or concentrated hydroiodic acid as a solvent. Chemical compositions were estimated by standard CHN combustion analysis for the organic part and by the Schöniger method for Br and I (by titrimetric analysis, Supplementary Table 5). The resulting compositions of SCs are proportional to the mixing ratios in the mother solution. Thermal analysis of $Cs_{0.1}FA_{0.9}PbI_{2.7}Br_{0.3}$ indicates satisfactory stability upon heating in inert atmosphere (Figure 1e). For instance, decomposition does not occur until above 300 °C, a similar case to pure $FAPbI_3$.[34,41] Two steps of mass loss were observed. A total gravimetric loss of 20% occurs between 316–370 °C, corresponding to the removal of FA-halide (for example, conversion into $Cs_{0.1}PbX_{2+x}$). Lead halides then evaporate above 500 °C, leaving CsX residue. In comparison, the removal of the organic part from the methylammonium counterpart, $CH_3NH_3PbI_3$, already occurs at 150–200 °C.[55–57] The powder X-ray diffraction (XRD) pattern of the parent $FAPbI_3$ SC (Supplementary Figure 3) indicates phase-pure α-$FAPbI_3$ with cubic symmetry, consistent with previously reported crystallographic data.[21,58] All compositions of $Cs_xFA_{1-x}PbI_{3-y}Br_y$ ($x = 0$–0.1, $y = 0$–0.6) exhibited the same general XRD pattern, without any detectable crystalline impurities (Supplementary Figure 4a). The formation of solid solutions is clearly visible by the shifts of the XRD reflections, as exemplified in Figure 1d for the (100) reflection. With the simultaneous replacement of FA and I ions with smaller Cs and Br ions, an expected systematic shift to higher angles without any apparent broadening was observed, confirming the decrease in the lattice constant. To within the instrumental resolution of our powder X-ray diffractometer, ground perovskite SCs, obtained in this work, exhibit same degree of crystallinity as highly crystalline Si (Supplementary Figures 4b and c). Such a shift is also detectable, although to a lesser extent, with the exchange of FA by Cs only (that is,

without alteration of the halide composition, Supplementary Figure 5). Powder XRD was then also used to monitor the phase stability of the SCs grown in this work. In these experiments, all samples were handled under ambient conditions, but stored in a desiccator over calcium chloride to ensure standardized humidity conditions during storage. SCs of α-$FAPbI_3$ transformed into a yellow hexagonal phase within 24 h, in agreement with earlier reports.[21,41] The replacement of 10% of the FA ions by Cs led to much higher stability, with the first signs of degradation (minor XRD peaks corresponding to hexagonal $FAPbI_3$) seen only after 20 days of storage. When also Br ions are added, that is, to form quinary compositions, the stability could be further improved to at least 2 months of storage (for example, at $y = 0.2$–0.4, Supplementary Figure 6).

Optical properties

The facile synthesis of solid solutions of $Cs_xFA_{1-x}PbI_{3-y}Br_y$ ($x = 0$–0.1, $y = 0$–0.6) lends itself to measurements of their optical properties, wherein the continuous compositional variation manifests in the continuous evolution of optical absorption and photoluminescence spectra (varying y shown in Figures 2a–c, and varying x in Supplementary Figure 7). A bandgap of 1.43 eV (the narrowest measured herein) and a photoluminescence maximum at 840 nm is found for the reference sample of α-$FaPbI_3$ (Figures 2a and b), in agreement with the literature.[34,42,44] The incorporation of either Cs, Br or both increases the bandgap energy (Figure 2b). In general, the bandgap of the three-dimensional $APbX_3$-perovskites scales either with the nature of the halide ion (the electronegativity effect) or with geometric factors (for example, the tilting angle between PbX_6 octahedra, compressive/tensile strain and so on).[59] The effect of substitutional Cs-doping (Figure 2c, Supplementary Figure 7) in $FAPbI_3$ can be ascribed to fine geometric effects. The replacement of FA with Cs may also influence the spin-orbit effects in this lattice.[60] The dependence of bandgap on composition reported in this work is also consistent with numerous recent thin-film studies in photovoltaic research.[47,49–51] It should be emphasized that the convenient tuning of the absorption onset to shorter wavelengths of 700–750 nm is potentially highly advantageous for the construction of tandem solar cells.[61–64]

Absorption and detection of gamma photons in hybrid perovskite SCs

Upon the substitutional doping of $FAPbI_3$ SCs by Cs and Br, not only does the crystalline phase stability increase and the optical absorption shift to lower wavelength, but also the electronic parameters such as dark current and shot noise are affected. In particular, the higher the bandgap is, the greater are the dark currents (see specific resistivity of SCs of various compositions in Supplementary Figure 8) and noise levels in the studied systems (not generally expected).

Taking into account this trade-off between the doping level and the corresponding electronic characteristics, we have focused on SCs with a composition of $x = 0.1$ and $y = 0.2$ (that is, 10% of Cs and 10% of $PbBr_2$) in subsequent gamma-detection studies.

The absorption of X-rays and gamma radiation in high-Z semiconductor materials can be described by several processes: photoionization, Compton scattering and electron-positron pair creation.[40] We performed a calculation of the absorption (α) of high-energy photons by SCs with the composition $Cs_{0.1}FA_{0.9}PbI_{2.8}Br_{0.2}$ in the photon energy range of 20–1000 keV (Figure 3a). The resulting absorptivity spectrum contains two resonant absorption peaks due to transitions involving the core electron levels of constituting atoms, so-called $K\alpha$ lines, a long, monotonically decreasing photoelectric tail and a component responsible for electron-positron pair creation at higher energies (>1 MeV). We then verified the accuracy of these calculations by measurements of the absorption of gamma radiation from two sources (^{241}Am and ^{137}Cs) by several 0.2–15 mm thick SCs, and the results are presented as two points in Figure 3a. From the penetration depth (calculated as the inverse of absorption), it is apparent that emission from the ^{241}Am source ($E_\gamma = 59.6$ keV) at rather low gamma photon energies can be absorbed by a 1 mm sized SC. Comparatively, a 10 times larger (1 cm) SC absorbed only ~30% of the intensity of gamma radiation from a ^{137}Cs source ($E_\gamma = 662$ keV). With such large SCs, the efficiency of carrier separation and collection becomes a major concern. It was recently shown that a drift length in the mm range can be accomplished in $MAPbBr_3$ SCs.[12] Charge collection efficiency can be evaluated from the dependence of the photocurrent on bias (Figure 3b), with the aid of the Hecht model.[65,66] This directly yields a figure-of-merit known as the carrier mobility–lifetime product ($\mu\tau$).[40] This parameter increases drastically for SCs[15] as compared to polycrystalline perovskites.[11] In this study, a median value of $\mu\tau = 0.04\ cm^2\ V^{-1}$ was found for SCs of $Cs_{0.1}FA_{0.9}PbI_{2.8}Br_{0.2}$, whereas the champion SC showed a value of $\mu\tau = 0.12\ cm^2\ V^{-1}$. These values correspond well to the best reported $\mu\tau$ values for CdTe-based SCs.

In this work and in a previous study,[14] we find that with lead halide perovskites the charge collection efficiency is primarily limited by the bias-stability of the SCs. Due to ionic migration in perovskites, also known to cause hysteresis and other instabilities in photovoltaic solar cells,[67] the highest bias at which the dark current and noise are not significantly affected is in the range of 5–30 V, being highest for FA-based SCs and lowest for $MAPbI_3$ SCs. Based on these values, we have estimated a drift length (Figure 3b), also known as a *schubweg*,[40] calculated as $\mu\tau E$, where E is the applied electric field. For optimal charge collection, the penetration depth of a gamma photon of a certain energy must not exceed the drift length; that is, $\alpha\mu\tau E \geqslant 1$. This assumes that the electric field (that is, the trajectories of the collected carriers) is parallel to the gamma flux. At the higher allowed biases in FA perovskites, the calculated drift length reaches 1.7 cm, meaning that at photon energies lower than 400 keV the penetration depth will not exceed the drift length. The condition of $\alpha\mu\tau E \geqslant 1$ for drift lengths of 1.7 cm is graphically represented as a shaded green area in Figure 3a. Only within this area should a given SC be able to efficiently collect the charge carrier. Efficient charge carrier collection is also a precondition for obtaining energy-resolved spectra, based on pulse-height analysis. The latter aspect can be illustrated by performing a pulse-height analysis of the signals from two gamma sources: ^{241}Am (Figure 3c) and ^{137}Cs (Figure 3d). Clearly, the better energy-resolving capability of perovskite SCs is obtained at lower energies, that is, within the range of efficient charge collection.

DISCUSSION

ABX_3 perovskites are composed of BX_6 octahedra, connected by corner-sharing in three dimensions. One such compound, α-$FAPbI_3$ exhibits a highly symmetric cubic *Pm-3m* lattice with a unit cell parameter of $a = 6.3620(8)$ Å (Figure 1a).[21,58] However, at room temperature this lattice undergoes a phase transformation into a hexagonal $P6_3mc$ crystal structure, consisting of single one-dimensional chains of face-sharing PbI_6 octahedra and FA cations situated in between the chains (Figure 1b).[41] The three-dimensional electronic delocalization is therefore broken, deteriorating its semiconductive properties and drastically increasing the bandgap. Sometimes this phase is simply referred to as a 'yellow phase' due to its color. Only at elevated temperatures of 185 °C does the hexagonal $FAPbI_3$ transform into the black α-$FAPbI_3$.[34] This black phase is

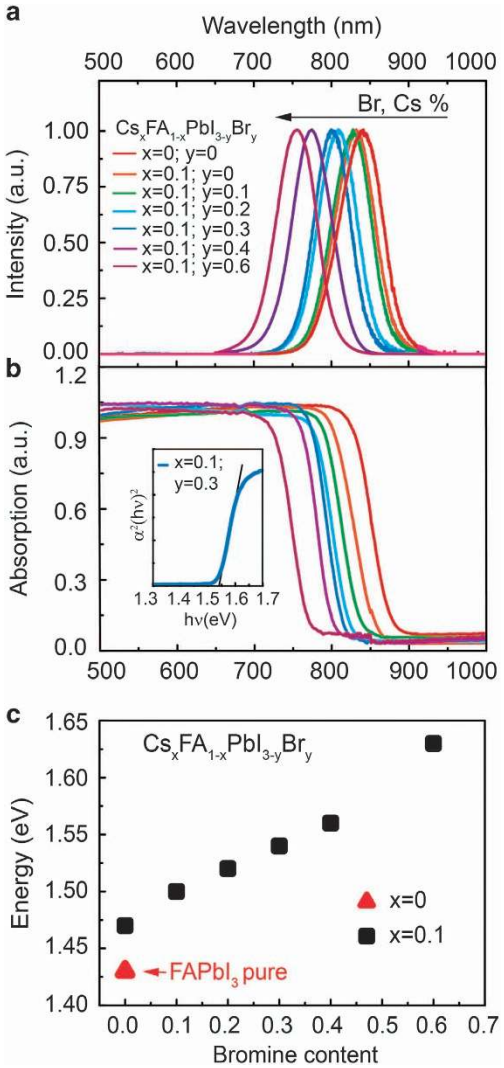

Figure 2 Optical properties of $Cs_xFA_{1-x}PbI_{3-y}Br_y$ ($x=0$–0.1, $y=0$–0.6) SCs. (**a**) Room-temperature photoluminescence spectra of ground SCs. (**b**) Absorption spectra of SCs held between two glass plates. (**c**) Bandgap energy as a function of Br content for compositions of fixed Cs content ($x=0.1$). SC, single crystal.

obtained as a SC upon synthesis from a hot solution at 130 °C, but then quickly undergoes a phase transition to the yellow phase at room temperature.[21,33,34] The primary goal of this work was to prevent this phase transition through compositional variations within the $FAPbI_3$ lattice: by replacing FA cations with up to 10% of Cs, and I anions with up to 30% of Br. The compositionally dependent stability of perovskites can be semi-quantitatively rationalized using the Goldsmith tolerance factor (GTF) concept, initially proposed for metal-oxide perovskites[68] and recently extended to metal halides.[51,69–71] The GTF of a three-dimensional perovskite with ABX_3 composition and idealized cubic lattice can be calculated as:

$$\mathrm{GTF} = \frac{(r_A + r_X)}{\sqrt{2}(r_B + r_X)}$$

where r_A, r_B and r_X represent the ionic radii of each lattice site constituent (in this case, $r_{FA^+} = 253$ pm, $r_{Pb^{2+}} = 119$ pm and $r_{I^-} = 220$ pm). Stable cubic perovskites of formula ABX_3 are expected to exhibit a GTF between 0.8 and 1,[51,69,72] which explains the instability of α-$FAPbI_3$ at room temperature (GTF≈1). It should be noted that the non-spherical geometry of the FA cation complicates the analysis.[73] Clearly, the GTF can be decreased by replacing FA cations by smaller Cs ions and/or by replacing I anions with smaller Br ions, likely leading to higher stabilities. These possibilities have been successfully tested in this work, leading to greatly increased phase stabilities of the perovskite SCs, as evidenced by an extended shelf-life of up to at least several months without any detectable traces of other crystalline phases (Supplementary Figure 6). The most preferred scenario in the context of gamma-sensing is FA-to-Cs exchange, as it has minimal effect on the bandgap energy and incorporates a heavy atom, which is highly desirable for the absorption of gamma photons. In addition, up to 30% of the I sites could be simultaneously substituted with Br ions. Both cationic and anionic exchanges manifested themselves as changes in the bandgap energy. $Cs_{0.1}FA_{0.9}PbI_3$ exhibits a 0.05 eV higher bandgap than α-$FAPbI_3$, whereas a further increase by 0.2 eV can be seen upon the incorporation of 30% Br, that is, for $Cs_{0.1}FA_{0.9}PbI_{2.4}Br_{0.6}$. Besides Cs- and concomitant Cs/Br substitutional doping, doping of the halide site only, for example, in the formation of $FAPbI_{3-x}Br_x$, has been successful as well and will be reported elsewhere. We note a good proportionality between the I:Br and Cs:FA ratios in the mother solution and in the resulting SCs (Supplementary Table 5), with the general trend being that bromide contents are higher in the SCs.

With thermodynamically stable and large $Cs_xFA_{1-x}PbI_{3-y}Br_y$ SCs at our disposal, we then tested their gamma-photon-sensing properties and compared them to our earlier work on $MAPbI_3$.[14] Besides the thermodynamic phase stability and chemical stability that both determine the shelf-life of the SCs, the operational stability due to the effects of polarization and ionic motion[74,75] also becomes an important issue for practical gamma detection. $Cs_xFA_{1-x}PbI_{3-y}Br_y$ SCs exhibit a much higher operational stability than $MAPbI_3$, as can be seen from the continuous gamma-counting measurement under applied voltage bias (Figure 4a). The counting rates of all three compositions compared in Figure 4 fall within the same order of magnitude, with $Cs_xFA_{1-x}PbI_{3-y}Br_y$ SCs exhibiting systematically 2–3 times higher values. The subtle decrease in sensitivity can be quickly recovered by applying a bias of opposite sign, suggesting that ionic migration is the major cause for the sensitivity decrease. Such improvements inspired us to design a simple and low-cost prototype of a gamma dosimeter, comprising the advantages of solution-grown SCs and the swiftly developing field of open-source microprocessor controllers. We applied open-source 'do-it-yourself' project (https://sites.google.com/site/diygeigercounter/) that uses standard Geiger gas tube as detector and Arduino microprocessor platform for digital counting board. We replaced the Geiger counter with perovskite SC solid-state gamma detector (Figure 4b) and a commercial charge-sensitive preamplifier (Figure 4c). The resulting assembly exhibits a strong response to a ^{137}Cs gamma radiation source of rather low activity (2.2 MBq), as illustrated by Figures 4c and d and by Supplementary Video 1. These devices were assembled and handled under ambient conditions. The long-term operation of such dosimeters is directly determined by the chemical integrity of the perovskite SCs, ranging from, at best, several days for $FAPbI_3$ to several months for $Cs_xFA_{1-x}PbI_{3-y}Br_y$ SCs.

In conclusion, we have presented a simple solution-growth method to synthesize quaternary $Cs_xFA_{1-x}PbI_3$ and quinary $Cs_xFA_{1-x}PbI_{3-y}Br_y$ ($x \leqslant 0.1$, $y \leqslant 0.6$) SCs with excellent long-term thermodynamic stability. Such materials present an attractive alternative to $MAPbX_3$ compounds, which are prone to decomposition into PbX_2 and MAX.[76] With very high mobility–lifetime products of

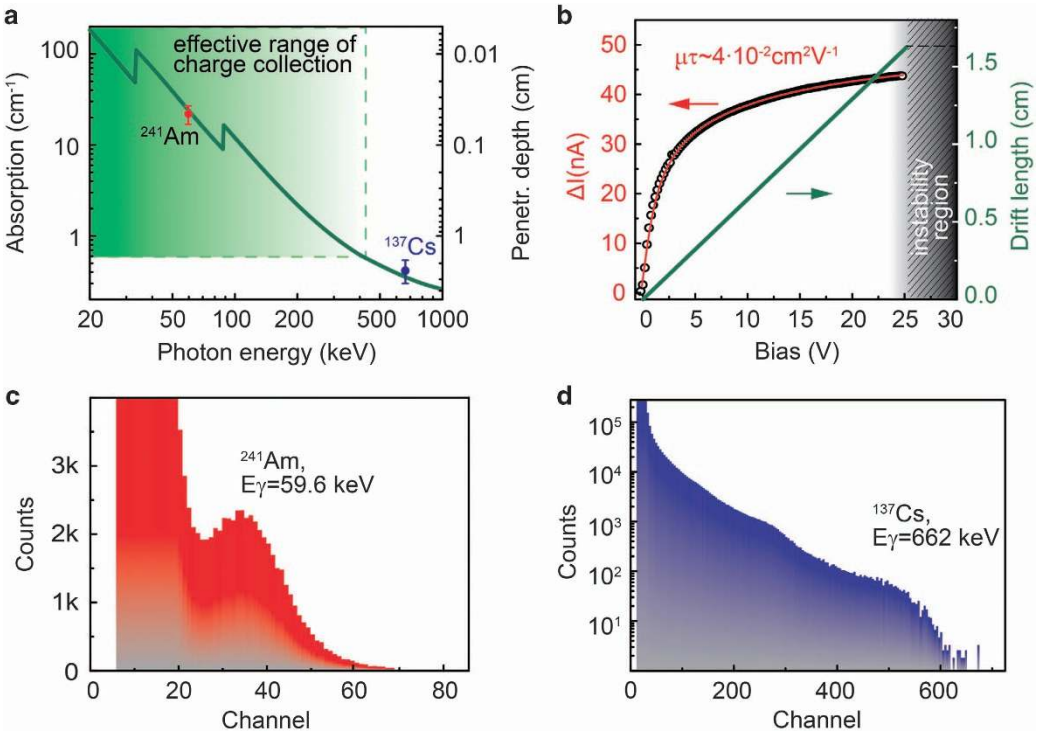

Figure 3 Response of $Cs_{0.1}FA_{0.9}PbI_{2.8}Br_{0.2}$ SC to gamma-rays. (**a**) Absorption and penetration depth as a function of photon energy, showing the calculated spectrum (green line) and measured values (red and blue symbols). The shaded green area indicates the effective range of charge collection, within which the penetration depth corresponds to the charge collection distance at the maximum applied bias of 25 V. (**b**) Evaluation of $\mu\tau$ from the dependence of photocurrent on bias, and the corresponding effective distance of charge collection. (**c** and **d**) Energy-resolved spectra of gamma detection from an ^{241}Am and a ^{137}Cs source, respectively. SC, single crystal.

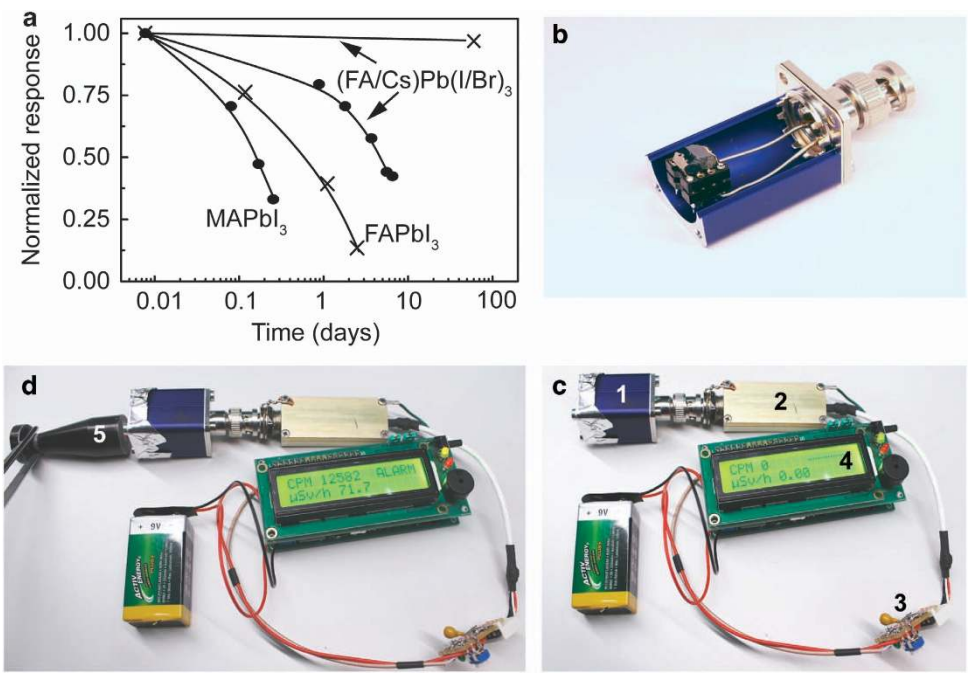

Figure 4 Prototype of a gamma dosimeter based on $Cs_{0.1}FA_{0.9}PbI_{2.8}Br_{0.2}$ SC. (**a**) Operational stability (crosses) and storage stability (circles) of $Cs_{0.1}FA_{0.9}PbI_{2.8}Br_{0.2}$ SCs compared to $MAPbI_3$ and $FAPbI_3$ SCs. (**b**) Detail photograph of the detector fixture with an installed $FAPbI_3$ or $Cs_{0.1}FA_{0.9}PbI_{2.8}Br_{0.2}$ SC. Photographs of the complete device during measurement (**c**) in the absence of a gamma radiation source and (**d**) in the presence of a ^{137}Cs source (activity = 2.2 MBq). The labels correspond to: 1—detector crystal fixture, 2—charge-sensitive preamplifier (from eV products), 3—amplifier, 4—digital counting board using an Arduino microprocessor set, based on an open-source project (https://sites.google.com/site/diygeigercounter/) and 5—^{137}Cs source. SC, single crystal.

up to 1.2×10^{-1} cm^2 V^{-1}, such high-Z semiconductor SCs exhibit a high sensitivity to gamma photons, allowing single-photon counting and inexpensive dosimetry. Besides hard radiation detection as presented herein, we expect that owing to their compositionally tunable bandgap energies, these SCs will attract further research activities toward investigating their applications in photodetectors operating in the visible and infrared regions, as well as in fundamental studies of the charge transport and photophysics of these novel semiconductors.

CONFLICT OF INTEREST

The authors declare no conflict of interest.

ACKNOWLEDGEMENTS

MVK acknowledges financial support from the European Union through the FP7 (ERC Starting Grant NANOSOLID, GA No. 306733). Elemental analysis was performed at the Laboratory of Microelemental Analysis of ETH Zurich. We thank Michael Wörle for assistance with crystal structure refinement and Nicholas P Stadie for reading the manuscript. We also thank Prof. Mark Weller for providing the cif file of the $FAPbI_3$ cubic phase.

Author contributions: MVK conceived and supervised the work. ON, VM and IC prepared the samples and performed XRD and optical spectroscopy characterization, and SY performed measurements of the response of perovskite SCs to visible light and gamma-rays and designed and constructed the dosimeter prototype. ON performed thermal analysis and single-crystal structure determination. ON, SY and MK wrote the manuscript. All authors discussed the results and commented on the manuscript.

1 Mitzi, D. B. *Progress in inorganic chemistry* 1–121 (John Wiley & Sons, Inc., New York, NY, USA, 2007).
2 Park, N.-G. Perovskite solar cells: an emerging photovoltaic technology. *Mater. Today* **18**, 65–72 (2015).
3 Lee, M. M., Teuscher, J., Miyasaka, T., Murakami, T. N. & Snaith, H. J. Efficient hybrid solar cells based on meso-superstructured organometal halide perovskites. *Science* **338**, 643–647 (2012).
4 Gratzel, M. The light and shade of perovskite solar cells. *Nat. Mater.* **13**, 838–842 (2014).
5 Green, M. A., Ho-Baillie, A. & Snaith, H. J. The emergence of perovskite solar cells. *Nat. Photon.* **8**, 506–514 (2014).
6 Tan, Z.-K., Moghaddam, R. S., Lai, M. L., Docampo, P., Higler, R., Deschler, F., Price, M., Sadhanala, A., Pazos, L. M., Credgington, D., Hanusch, F., Bein, T., Snaith, H. J. & Friend, R. H. Bright light-emitting diodes based on organometal halide perovskite. *Nat. Nanotechnol.* **9**, 687–692 (2014).
7 Xing, G., Mathews, N., Lim, S. S., Yantara, N., Liu, X., Sabba, D., Grätzel, M., Mhaisalkar, S. & Sum, T. C. Low-temperature solution-processed wavelength-tunable perovskites for lasing. *Nat. Mater.* **13**, 476–480 (2014).
8 Zhu, H., Fu, Y., Meng, F., Wu, X., Gong, Z., Ding, Q., Gustafsson, M. V., Trinh, M. T., Jin, S. & Zhu, X. Y. Lead halide perovskite nanowire lasers with low lasing thresholds and high quality factors. *Nat. Mater.* **14**, 636–642 (2015).
9 Dou, L., Yang, Y., You, J., Hong, Z., Chang, W.-H., Li, G. & Yang, Y. Solution-processed hybrid perovskite photodetectors with high detectivity. *Nat. Commun.* **5**, 5404 (2014).
10 Fang, Y., Dong, Q., Shao, Y., Yuan, Y. & Huang, J. Highly narrowband perovskite single-crystal photodetectors enabled by surface-charge recombination. *Nat. Photon.* **9**, 679–686 (2015).
11 Yakunin, S., Sytnyk, M., Kriegner, D., Shrestha, S., Richter, M., Matt, G. J., Azimi, H., Brabec, C. J., Stangl, J., Kovalenko, M. V. & Heiss, W. Detection of X-ray photons by solution-processed lead halide perovskites. *Nat. Photon.* **9**, 444–449 (2015).
12 Wei, H., Fang, Y., Mulligan, P., Chuirazzi, W., Fang, H.-H., Wang, C., Ecker, B. R., Gao, Y., Loi, M. A., Cao, L. & Huang, J. Sensitive X-ray detectors made of methylammonium lead tribromide perovskite single crystals. *Nat. Photon.* **10**, 333–339 (2016).
13 Náfrádi, B., Náfrádi, G., Forró, L. & Horváth, E. Methylammonium lead iodide for efficient x-ray energy conversion. *J. Phys. Chem. C* **119**, 25204–25208 (2015).
14 Yakunin, S., Dirin, D. N., Shynkarenko, Y., Morad, V., Cherniukh, I., Nazarenko, O., Kreil, D., Nauser, T. & Kovalenko, M. V. Detection of gamma photons using solution-grown single crystals of hybrid lead halide perovskites. *Nat. Photon.* **10**, 585–589 (2016).
15 Dong, Q., Fang, Y., Shao, Y., Mulligan, P., Qiu, J., Cao, L. & Huang, J. Electron-hole diffusion lengths >175 μm in solution-grown $CH_3NH_3PbI_3$ single crystals. *Science* **347**, 967–970 (2015).
16 Zakutayev, A., Caskey, C. M., Fioretti, A. N., Ginley, D. S., Vidal, J., Stevanovic, V., Tea, E. & Lany, S. Defect tolerant semiconductors for solar energy conversion. *J. Phys. Chem. Lett.* **5**, 1117–1125 (2014).
17 Brandt, R. E., Stevanović, V., Ginley, D. S. & Buonassisi, T. Identifying defect-tolerant semiconductors with high minority-carrier lifetimes: beyond hybrid lead halide perovskites. *MRS Commun.* **5**, 265–275 (2015).
18 Manser, J. S., Christians, J. A. & Kamat, P. V. Intriguing optoelectronic properties of metal halide perovskites. *Chem. Rev.* **116**, 12956–13008 (2016).
19 Buin, A., Pietsch, P., Xu, J., Voznyy, O., Ip, A. H., Comin, R. & Sargent, E. H. Materials processing routes to trap-free halide perovskites. *Nano Lett.* **14**, 6281–6286 (2014).
20 Shi, D., Adinolfi, V., Comin, R., Yuan, M., Alarousu, E., Buin, A., Chen, Y., Hoogland, S., Rothenberger, A., Katsiev, K., Losovyj, Y., Zhang, X., Dowben, P. A., Mohammed, O. F., Sargent, E. H. & Bakr, O. M. Low trap-state density and long carrier diffusion in organolead trihalide perovskite single crystals. *Science* **347**, 519–522 (2015).
21 Zhumekenov, A. A., Saidaminov, M. I., Haque, M. A., Alarousu, E., Sarmah, S. P., Murali, B., Dursun, I., Miao, X.-H., Abdelhady, A. L., Wu, T., Mohammed, O. F. & Bakr, O. M. Formamidinium lead halide perovskite crystals with unprecedented long carrier dynamics and diffusion length. *ACS Energy Lett.* **1**, 32–37 (2016).
22 Hao, F., Stoumpos, C. C., Chang, R. P. H. & Kanatzidis, M. G. Anomalous band gap behavior in mixed Sn and Pb perovskites enables broadening of absorption spectrum in solar cells. *J. Am. Chem. Soc.* **136**, 8094–8099 (2014).
23 Lian, Z., Yan, Q., Gao, T., Ding, J., Lv, Q., Ning, C., Li, Q. & Sun, J.-l. Perovskite $CH_3NH_3PbI_3$(Cl) single crystals: rapid solution growth, unparalleled crystalline quality, and low trap density toward 10^8 cm^{-3}. *J. Am. Chem. Soc.* **138**, 9409–9412 (2016).
24 Xing, G., Mathews, N., Sun, S., Lim, S. S., Lam, Y. M., Grätzel, M., Mhaisalkar, S. & Sum, T. C. Long-range balanced electron- and hole-transport lengths in organic-inorganic $CH_3NH_3PbI_3$. *Science* **342**, 344–347 (2013).
25 Dang, Y., Ju, D., Wang, L. & Tao, X. Recent progress in the synthesis of hybrid halide perovskite single crystals. *CrystEngComm* **18**, 4476–4484 (2016).
26 Huang, J., Shao, Y. & Dong, Q. Organometal trihalide perovskite single crystals: a next wave of materials for 25% efficiency photovoltaics and applications beyond? *J. Phys. Chem. Lett.* **6**, 3218–3227 (2015).
27 Zhang, W., Saliba, M., Moore, D. T., Pathak, S. K., Hörantner, M. T., Stergiopoulos, T., Stranks, S. D., Eperon, G. E., Alexander-Webber, J. A., Abate, A., Sadhanala, A., Yao, S., Chen, Y., Friend, R. H., Estroff, L. A., Wiesner, U. & Snaith, H. J. Ultrasmooth organic-inorganic perovskite thin-film formation and crystallization for efficient planar heterojunction solar cells. *Nat. Commun.* **6**, 7142 (2015).
28 Yang, S., Wang, Y., Liu, P., Cheng, Y.-B., Zhao, H. J. & Yang, H. G. Functionalization of perovskite thin films with moisture-tolerant molecules. *Nat. Energy* **1**, 15016 (2016).
29 Zhang, F., Zhong, H., Chen, C., Wu, X.-g., Hu, X., Huang, H., Han, J., Zou, B. & Dong, Y. Brightly luminescent and color-tunable colloidal $CH_3NH_3PbX_3$ (X = Br, I, Cl) quantum dots: potential alternatives for display technology. *ACS Nano* **9**, 4533–4542 (2015).
30 Vybornyi, O., Yakunin, S. & Kovalenko, M. V. Polar-solvent-free colloidal synthesis of highly luminescent alkylammonium lead halide perovskite nanocrystals. *Nanoscale* **8**, 6278–6283 (2016).
31 Saidaminov, M. I., Abdelhady, A. L., Murali, B., Alarousu, E., Burlakov, V. M., Peng, W., Dursun, I., Wang, L., He, Y., Maculan, G., Goriely, A., Wu, T., Mohammed, O. F. & Bakr, O. M. High-quality bulk hybrid perovskite single crystals within minutes by inverse temperature crystallization. *Nat. Commun.* **6**, 7586 (2015).
32 Fang, H.-H., Raissa, R., Abdu-Aguye, M., Adjokatse, S., Blake, G. R., Even, J. & Loi, M. A. Photophysics of organic-inorganic hybrid lead iodide perovskite single crystals. *Adv. Funct. Mater.* **25**, 2378–2385 (2015).
33 Saidaminov, M. I., Abdelhady, A. L., Maculan, G. & Bakr, O. M. Retrograde solubility of formamidinium and methylammonium lead halide perovskites enabling rapid single crystal growth. *Chem. Commun.* **51**, 17658–17661 (2015).
34 Han, Q., Bae, S. H., Sun, P., Hsieh, Y. T., Yang, Y. M., Rim, Y. S., Zhao, H., Chen, Q., Shi, W. & Li, G. Single crystal formamidinium lead iodide ($FAPbI_3$): Insight into the structural, optical, and electrical properties. *Adv. Mater.* **28**, 2253–2258 (2016).
35 Liu, Y., Sun, J., Yang, Z., Yang, D., Ren, X., Xu, H., Yang, Z. & Liu, S. 20-mm-large single-crystalline formamidinium-perovskite wafer for mass production of integrated photodetectors. *Adv. Opt. Mater.* **4**, 1829–1837 (2016).
36 Saidaminov, M. I., Haque, M. A., Almutlaq, J., Sarmah, S., Miao, X.-H., Begum, R., Zhumekenov, A. A., Dursun, I., Cho, N., Murali, B., Mohammed, O. F., Wu, T. & Bakr, O. M. Inorganic lead halide perovskite single crystals: phase-selective low-temperature growth, carrier transport properties, and self-powered photodetection. *Adv. Opt. Mater.* **5**, 1600704 (2016).
37 Dirin, D. N., Cherniukh, I., Yakunin, S., Shynkarenko, Y. & Kovalenko, M. V. Solution-grown $CsPbBr_3$ perovskite single crystals for photon detection. *Chem. Mater.* **28**, 8470–8474 (2016).
38 Takahashi, T. & Watanabe, S. Recent progress in CdTe and CdZnTe detectors. *IEEE Trans. Nucl. Sci.* **48**, 950–959 (2001).
39 Eisen, Y. & Shor, A. CdTe and CdZnTe materials for room-temperature X-ray and gamma ray detectors. *J. Cryst. Growth* **184**, 1302–1312 (1998).
40 Schlesinger, T. E., Toney, J. E., Yoon, H., Lee, E. Y., Brunett, B. A., Franks, L. & James, R. B. Cadmium zinc telluride and its use as a nuclear radiation detector material. *Mater. Sci. Eng. R Rep.* **32**, 103–189 (2001).
41 Stoumpos, C. C., Malliakas, C. D. & Kanatzidis, M. G. Semiconducting tin and lead iodide perovskites with organic cations: phase transitions, high mobilities, and near-infrared photoluminescent properties. *Inorg. Chem.* **52**, 9019–9038 (2013).
42 Eperon, G. E., Stranks, S. D., Menelaou, C., Johnston, M. B., Herz, L. M. & Snaith, H. J. Formamidinium lead trihalide: a broadly tunable perovskite for efficient planar heterojunction solar cells. *Energy Environ. Sci.* **7**, 982–988 (2014).

43 Yang, W. S., Noh, J. H., Jeon, N. J., Kim, Y. C., Ryu, S., Seo, J. & Seok, S. I. High-performance photovoltaic perovskite layers fabricated through intramolecular exchange. *Science* **348**, 1234–1237 (2015).
44 Koh, T. M., Fu, K., Fang, Y., Chen, S., Sum, T. C., Mathews, N., Mhaisalkar, S. G., Boix, P. P. & Baikie, T. Formamidinium-containing metal-halide: an alternative material for near-ir absorption perovskite solar cells. *J. Phys. Chem. C* **118**, 16458–16462 (2014).
45 Fang, H.-H., Wang, F., Adjokatse, S., Zhao, N. & Loi, M. A. Photoluminescence enhancement in formamidinium lead iodide thin films. *Adv. Funct. Mater.* **26**, 4653–4659 (2016).
46 Ma, F., Li, J., Li, W., Lin, N., Wang, L. & Qiao, J. Stable alpha/delta phase junction of formamidinium lead iodide perovskites for enhanced near-infrared emission. *Chem. Sci.* **8**, 800–805 (2017).
47 McMeekin, D. P., Sadoughi, G., Rehman, W., Eperon, G. E., Saliba, M., Hörantner, M. T., Haghighirad, A., Sakai, N., Korte, L., Rech, B., Johnston, M. B., Herz, L. M. & Snaith, H. J. A mixed-cation lead mixed-halide perovskite absorber for tandem solar cells. *Science* **351**, 151–155 (2016).
48 Jeon, N. J., Noh, J. H., Yang, W. S., Kim, Y. C., Ryu, S., Seo, J. & Seok, S. I. Compositional engineering of perovskite materials for high-performance solar cells. *Nature* **517**, 476–480 (2015).
49 Yi, C., Luo, J., Meloni, S., Boziki, A., Ashari-Astani, N., Gratzel, C., Zakeeruddin, S. M., Rothlisberger, U. & Gratzel, M. Entropic stabilization of mixed A-cation ABX_3 metal halide perovskites for high performance perovskite solar cells. *Energy Environ. Sci.* **9**, 656–662 (2016).
50 Lee, J.-W., Kim, D.-H., Kim, H.-S., Seo, S.-W., Cho, S. M. & Park, N.-G. Formamidinium and cesium hybridization for photo- and moisture-stable perovskite solar cell. *Adv. Energy Mater.* **5**, 1501310 (2015).
51 Li, Z., Yang, M., Park, J.-S., Wei, S.-H., Berry, J. J. & Zhu, K. Stabilizing perovskite structures by tuning tolerance factor: formation of formamidinium and cesium lead iodide solid-state alloys. *Chem. Mater.* **28**, 284–292 (2016).
52 Smith, N. O. Retrograde solubility. *J. Chem. Educ.* **51**, 555 (1974).
53 Liu, Y., Zhang, Y., Yang, Z., Yang, D., Ren, X., Pang, L. & Liu, S. Thinness- and shape-controlled growth for ultrathin single-crystalline perovskite wafers for mass production of superior photoelectronic devices. *Adv. Mater.* **28**, 9204–9209 (2016).
54 Liu, Y., Yang, Z., Cui, D., Ren, X., Sun, J., Liu, X., Zhang, J., Wei, Q., Fan, H., Yu, F., Zhang, X., Zhao, C. & Liu, S. Two-inch-sized perovskite $CH_3NH_3PbX_3$ (X=Cl, Br, I) crystals: growth and characterization. *Adv. Mater.* **27**, 5176–5183 (2015).
55 Juarez-Perez, E. J., Hawash, Z., Raga, S. R., Ono, L. K. & Qi, Y. Thermal degradation of $CH_3NH_3PbI_3$ perovskite into NH_3 and CH_3I gases observed by coupled thermogravimetry-mass spectrometry analysis. *Energy Environ. Sci.* **9**, 3406–3410 (2016).
56 Deretzis, I., Alberti, A., Pellegrino, G., Smecca, E., Giannazzo, F., Sakai, N., Miyasaka, T. & La Magna, A. Atomistic origins of $CH_3NH_3PbI_3$ degradation to PbI_2 in vacuum. *Appl. Phys. Lett.* **106**, 131904 (2015).
57 Conings, B., Drijkoningen, J., Gauquelin, N., Babayigit, A., D'Haen, J., D'Olieslaeger, L., Ethirajan, A., Verbeeck, J., Manca, J., Mosconi, E., Angelis, F. D. & Boyen, H.-G. Intrinsic thermal instability of methylammonium lead trihalide perovskite. *Adv. Energy Mater.* **5**, 1500477 (2015).
58 Weller, M. T., Weber, O. J., Frost, J. M. & Walsh, A. Cubic perovskite structure of black formamidinium lead iodide, α-$[HC(NH_2)_2]PbI_3$, at 298 K. *J. Phys. Chem. Lett.* **6**, 3209–3212 (2015).
59 Stoumpos, C. C. & Kanatzidis, M. G. The renaissance of halide perovskites and their evolution as emerging semiconductors. *Acc. Chem. Res.* **48**, 2791–2802 (2015).
60 Amat, A., Mosconi, E., Ronca, E., Quarti, C., Umari, P., Nazeeruddin, M. K., Grätzel, M. & De Angelis, F. Cation-induced band-gap tuning in organohalide perovskites: interplay of spin-orbit coupling and octahedra tilting. *Nano Lett.* **14**, 3608–3616 (2014).
61 Albrecht, S., Saliba, M., Correa Baena, J. P., Lang, F., Kegelmann, L., Mews, M., Steier, L., Abate, A., Rappich, J., Korte, L., Schlatmann, R., Nazeeruddin, M. K., Hagfeldt, A., Gratzel, M. & Rech, B. Monolithic perovskite/silicon-heterojunction tandem solar cells processed at low temperature. *Energy Environ. Sci.* **9**, 81–88 (2016).
62 Fu, F., Feurer, T., Jager, T., Avancini, E., Bissig, B., Yoon, S., Buecheler, S. & Tiwari, A. N. Low-temperature-processed efficient semi-transparent planar perovskite solar cells for bifacial and tandem applications. *Nat. Commun.* **6**, 8932 (2015).
63 Werner, J., Weng, C.-H., Walter, A., Fesquet, L., Seif, J. P., De Wolf, S., Niesen, B. & Ballif, C. Efficient monolithic perovskite/silicon tandem solar cell with cell area $>1\ cm^2$. *J. Phys. Chem. Lett.* **7**, 161–166 (2016).
64 Bailie, C. D., Christoforo, M. G., Mailoa, J. P., Bowring, A. R., Unger, E. L., Nguyen, W. H., Burschka, J., Pellet, N., Lee, J. Z., Gratzel, M., Noufi, R., Buonassisi, T., Salleo, A. & McGehee, M. D. Semi-transparent perovskite solar cells for tandems with silicon and CIGS. *Energy Environ. Sci.* **8**, 956–963 (2015).
65 Street, R. A., Ready, S. E., Van Schuylenbergh, K., Ho, J., Boyce, J. B., Nylen, P., Shah, K., Melekhov, L. & Hermon, H. Comparison of PbI_2 and HgI_2 for direct detection active matrix x-ray image sensors. *J. Appl. Phys.* **91**, 3345–3355 (2002).
66 Kabir, M. Z. & Kasap, S. O. Charge collection and absorption-limited sensitivity of x-ray photoconductors: applications to a-Se and HgI_2. *Appl. Phys. Lett.* **80**, 1664–1666 (2002).
67 Snaith, H. J., Abate, A., Ball, J. M., Eperon, G. E., Leijtens, T., Noel, N. K., Stranks, S. D., Wang, J.T.-W., Wojciechowski, K. & Zhang, W. Anomalous hysteresis in perovskite solar cells.. *J. Phys. Chem. Lett.* **5**, 1511–1515 (2014).
68 Goldschmidt, V. M. Die Gesetze der Krystallochemie. *Naturwissenschaften* **14**, 477–485 (1926).
69 Kieslich, G., Sun, S. & Cheetham, A. K. An extended tolerance factor approach for organic-inorganic perovskites. *Chem. Sci.* **6**, 3430–3433 (2015).
70 Kieslich, G., Sun, S. & Cheetham, A. K. Solid-state principles applied to organic-inorganic perovskites: new tricks for an old dog. *Chem. Sci.* **5**, 4712–4715 (2014).
71 Filip, M. R., Eperon, G. E., Snaith, H. J. & Giustino, F. Steric engineering of metal-halide perovskites with tunable optical band gaps. *Nat. Commun.* **5**, 5757 (2014).
72 Saparov, B. & Mitzi, D. B. Organic-inorganic perovskites: structural versatility for functional materials design. *Chem. Rev.* **116**, 4558–4596 (2016).
73 Carignano, M. A., Saeed, Y., Aravindh, S. A., Roqan, I. S., Even, J. & Katan, C. A close examination of the structure and dynamics of $HC(NH_2)_2PbI_3$ by MD simulations and group theory. *Phys. Chem. Chem. Phys.* **18**, 27109–27118 (2016).
74 Meloni, S., Moehl, T., Tress, W., Franckevicius, M., Saliba, M., Lee, Y. H., Gao, P., Nazeeruddin, M. K., Zakeeruddin, S. M., Rothlisberger, U. & Graetzel, M. Ionic polarization-induced current-voltage hysteresis in $CH_3NH_3PbX_3$ perovskite solar cells. *Nat. Commun.* **7**, 10334 (2016).
75 Shao, Y., Xiao, Z., Bi, C., Yuan, Y. & Huang, J. Origin and elimination of photocurrent hysteresis by fullerene passivation in $CH_3NH_3PbI_3$ planar heterojunction solar cells. *Nat. Commun.* **5**, 6784 (2014).
76 Han, Y., Meyer, S., Dkhissi, Y., Weber, K., Pringle, J. M., Bach, U., Spiccia, L. & Cheng, Y.-B. Degradation observations of encapsulated planar $CH_3NH_3PbI_3$ perovskite solar cells at high temperatures and humidity. *J. Mater. Chem. A* **3**, 8139–8147 (2015).

Supplementary Information accompanies the paper on the NPG Asia Materials website (http://www.nature.com/am)